Measurement Science
and Technology

PAPER • **OPEN ACCESS**

Stereoscopic digital image correlation for hydroelastic waves of floating membranes

To cite this article: Hanna Pot *et al* 2025 *Meas. Sci. Technol.* **36** 125204

OPEN ACCESS
IOP Publishing
Measurement Science and Technology
Meas. Sci. Technol. **36** (2025) 125204 (17pp)
https://doi.org/10.1088/1361-6501/ae2348

Stereoscopic digital image correlation for hydroelastic waves of floating membranes

Hanna Pot[1,*], **Jerry Westerweel**[2] **and Sebastian Schreier**[1]

[1] Maritime and Transport Technology, Faculty of Mechanical Engineering, Delft University of Technology, Mekelweg 2, Delft, 2628 CD, The Netherlands
[2] Laboratory of Aero and Hydrodynamics, Faculty of Mechanical Engineering, Delft University of Technology, Mekelweg 2, 2628 CD Delft, The Netherlands

E-mail: h.m.pot@tudelft.nl, j.westerweel@tudelft.nl and s.schreier@tudelft.nl

Received 7 August 2025, revised 26 September 2025
Accepted for publication 24 November 2025
Published 30 December 2025

Abstract

Wave-structure interactions of flexible membrane-type materials are an emerging research field, driven by their potential in renewable energy and breakwater concepts. This study proposes stereoscopic digital image correlation (DIC) as a scalable method for spatiotemporal measurements of fluid-structure interactions in wave tanks. The scalability is presented by two setups with domain dimensions ranging from $O(10^{-1}\,\mathrm{m})$ to $O(10^{1}\,\mathrm{m})$. The calibrations of 5 adjacent and synchronized stereoscopic camera pairs are projected on a common frame of reference to cover the large domain. The presented methodology includes suggestions on the calibration method, and a practical speckle application technique is proposed. The benefits of the method are highlighted by the preliminary indication of a dynamic scaling law for wave-structure interactions. This work can serve as a foundation for further development and application of stereoscopic DIC for such structures. It is expected that this large domain method will contribute to further physical understanding of the fluid-structure interactions of large floating structures in waves.

Keywords: digital image correlation, fluid-structure interactions, very large floating structure, floating membranes, hydroelastic waves

1. Introduction

Membrane-type floating structures are promising solutions for breakwaters [1] and floating foundations for offshore photovoltaics [2, 3] as large surfaces can be covered and structural loads can be minimized. Recent research demonstrates that floating membranes can undergo variant deformation patterns in space and time depending on the wave condition [4, 5]. The numerical study by Agarwal *et al* [6] presents that the deformation amplitudes over the length of the membrane do not consistently decrease, increase or remain at a constant magnitude. In fact, the amplitude is influenced by a combination of factors, including the incident wave characteristics and the natural frequency of the system, and moreover changes over the length of the membrane. Further, an experimental study by Schreier and Jacobi [7] demonstrates a change in deformation amplitudes over the width of the model, and Sree *et al* [8] show attenuation over its length, as well as changes in wavelength, also called modulation.

These studies indicate that hydroelastic research of floating membranes includes wave attenuation, wave propagation,

* Author to whom any correspondence should be addressed.

and wave modulation. Wave modulation poses requirements on spatial resolution and attenuation on the out-of-plane amplitude and accuracy. Ultrasonic wave probes used in wave tanks often have an accuracy <1 mm (General Acoustics, Kiel, Germany). Therefore, a method is required that measures the full membrane domain with an out-of-plane accuracy ~ 1 mm for experimental research on wave-structure interactions of membranes.

For laboratory measurements on rigid offshore structures, accelerometers and rigid body motion tracking are often sufficient. However, since floating membranes may deform over their entire surface, high-resolution spatiotemporal measurement systems are required to capture their behavior. Up to now, the most used methods can be categorized as *motion tracking*, *stereoscopic-correlation*, *refraction*, *projection* and *reflection* methods, which are all optical methods. Motion tracking has been the first attempt to obtain motion measurements with a higher spatial resolution in a wave tank environment [9–12]. This method tracks the 3D position of individual markers with a system of multiple calibrated cameras. Despite its limited spatial resolution $O(10^{-1}\,\mathrm{m})$, the major advantages are its robustness against the overwash of water, and its capability of capturing large domains [12]. *Regular Grid Tracking* coarsely applies the same principles, and Orphin *et al* [13] improved the spatial resolution to $O(10^{-2}\,\mathrm{m})$ by applying a regular dot pattern.

More recently, stereoscopic correlation methods are used to further improve the spatial resolution in towing tank environments [7, 14, 15]. These methods capture the deformation of the surface by two cameras in a stereoscopic configuration and the presence of features, such as speckles on a surface, called digital image correlation (DIC), or particles in a flow, called particle image velocimetry [16]. A stereoscopic setup allows for the measurement of both in-plane and out-of-plane displacements. In the field of experimental mechanics, DIC is most commonly used. DIC measurements with extremely flexible models are already reported in the field of aero-elasticity, showing the possibility to derive an aeroelastic model from the spatiotemporal measurements [17]. As a downside, speckle application on delicate membranes could alter material properties. In a recent study, this is mitigated by projecting speckles on a surface [18]. Additionally, experiments with multicamera setups are conducted to enlarge the measurement domain. Here, the field of view (FoV) of individual cameras are combined [19]. So far, DIC measurements in wave tanks have been limited to single pair stereoscopic DIC configurations that capture part of the model [7, 15], or measure smaller sized models [14]. Schreier and Jacobi [7] achieved a larger domain by shifting the model through the FoV of the cameras and subsequently repeat the measurements. Although this procedure can reveal additional information, it is laborious. Moreover, results of different repetitions can hardly be stitched when incident waves hold variations over time or have a lesser repeatability in terms of amplitude, steepness and length, as is often seen for steeper waves. Besides, overwash of water can cause camera correspondence problems in wave tanks, jeopardizing the robustness of DIC [16].

Reflection-based methods, such as light detection and ranging (LiDAR), may be suitable to overcome the potential problem of overwash. LiDAR is used for wave field detection in both wave tank [20–22] and coastal applications [23]. The fast scanning mechanism offers the possibility to measure large domains at a high sampling rate: Streicher *et al* [20] reports a rate of 50 Hz for a FoV of $3\,\mathrm{m} \times 0.8\,\mathrm{m}$. Compared to DIC, LiDAR compromises on spatial resolution and out-of-plane accuracy. In contrast to stereoscopic correlation methods, LiDAR does not identify markers attached to the object itself, through which strain cannot be measured, and rigid body motions may be harder to derive from the measurements.

In small measurement domains $O(10^{-1}\,\mathrm{m})$ with fully transparent membranes, *Synthethic Schlieren* can be applied to measure hydroelastic interactions [24, 25]. This is an optical method that uses the refractive property of the fluid and obtains the deformation of the surface by means of correlation algorithms [26]. The convenience of this method lies in the use of a single camera, and the absence of calibration and speckle application to membrane, through which it is a fully non-intrusive method. Deformation with large curvatures or large water depths are limitations for this method due to the refractive limits [25, 26], as well as the small domain size itself.

On large scales, drone assisted photogrammetry is used for structural health monitoring of a deformed floating membrane cover [27]. This method uses a single drone to make a 3D elevation model of the structure. In contrast to our requirements, this method measures the static deformation instead of the dynamic deformations. Recent papers are published about dynamic deformation measurements with multiple drones. These methods are for instance used to measure the vibrations of bridges. A review paper by Marendić *et al* [28] states the value of these multi drone measurements, but also concludes on a lower accuracy than conventional photogrammetic methods. The drone-assisted methods focus on modal analysis derived from the displacement of a few markers on the object of interest, and are therefore not full-field methods. Also, these investigations do not focus on the out-of-plane deformations, and often do not assess it at all [29, 30]. Up to our knowledge, drone-assisted research either focuses on (quasi-) static deformations, or do not measure full displacement fields and out-of-plane displacements when assessing dynamic displacements.

An overview of conventional approaches for hydroelastic research is presented in table 1. This shows that up to now, none of the methods meet the domain and accuracy requirements to capture spatiotemporal deformations of floating membranes. However, DIC seems the most promising method to meet the requirements because of its scalable spatial and temporal resolution, as well as its 3D capabilities. So far, DIC measurements in towing tank environments have been limited to single pair stereoscopic DIC configurations. For full domain measurements of large structures, a multicamera DIC setup is needed. Although these setups have been reported [19], their suitability is neither studied in wave tanks, nor in the context of floating membranes in waves, which demands a limited uncertainty in the out-of-plane direction.

Table 1. Overview of measurement techniques for large domain and time resolved measurements of floating membranes in a 3D domain. The domain size is defined by the length L times the width B with the out of plane amplitude defined as the normal to the surface $L \times B$. Some data are estimated from the papers, denoted by *. Parameters that remain not defined and could not be estimated are denoted by (-).

	Domain size $(L \times B)$ [m^2]	Out of plane amplitude [mm]	Out of plane uncertainty [mm]	In plane spatial resolution [mm]
Motion tracking				
Montiel *et al* [9]	1.44×0.72	44	—	180
Meylan *et al* [10]	1×1	37	—	330
Yoon *et al* [11]	3×0.6	10	—	270–440
Michele *et al* [12]	1.5×0.75	30	—	180–400
Orphin *et al* [13]	0.33×0.25	40*	—	20
Stereoscopic-correlation				
Schreier and Jacobi [7]	1.8×1.8	20	$O(10^0)$	15
Kristiansen *et al* [14]	0.8×0.4	50	—	—
Pambela *et al* [15]	1.0×1.0	20	—	—
Projection-based				
Deike *et al* [31]	0.25×0.20	—	—	0.001
Refraction-based				
Ono-Dit-Biot *et al* [25]	0.20×0.16	1	—	—
Domino *et al* [24]	0.20×0.20	—	$O(10^{-3})$	0.7
LiDAR				
Streicher *et al* [20]	3×0.8	100	$O(10^1)$	10–27
Zhang *et al* [21]	5×0.5	128	$O(10^1)$	10–40
Blenkinsopp *et al* [22]	8×0.9	150	$O(10^1)$	15–55

This article studies the suitability of DIC for spatiotemporal measurements of hydroelastic waves. Two cases and setups are used in this paper: first, a setup with one stereoscopic camera pair is used for spatiotemporal analysis of unsteady floating membrane deformations, showing its potential for the derivation of dynamic scaling laws, and second, a large multicamera setup is used for spatiotemporal measurements of a 5 m$\times$1 m floating membrane in a wave tank. The multicamera setup consists of 5 side-by-side stereoscopic camera pairs, which allows for measurements on large aspect ratio models in the large domain of 5.0 m $\times$ 1.0 m $\times$ 0.2 m. The method is evaluated for displacement errors over the whole domain, since wave attenuation is evaluated over the entire membrane. In addition, a practical method for speckle application is presented, as well as an effective calibration procedure for large domains.

2. Theory

We consider a floating elastic sheet with sheet density ρ_s, Young's Modulus E, Poisson ration ν and thickness h. A uniform and isotropic tension T is present in the sheet, resulting in the following momentum equation [32–34]:

$$D\nabla^4\eta - T\nabla^2\eta + \rho_s h\frac{\partial^2\eta}{\partial t^2} = p, \tag{1}$$

where η is the surface normal sheet deformation, p is the pressure due to the fluid on the bottom surface of the elastic sheet, and the plate bending rigidity is defined as $D = Eh^3/(12(1-\nu^2))$. ∇^2 and ∇^4 are the Laplacian and bi-Laplacian operators, defined as $\nabla^2 = \partial^2/\partial x^2 + \partial^2/\partial y^2$ and $\nabla^4 = \partial^4/\partial x^4 + \partial^4/\partial y^4 + \partial^4/\partial x^2\partial y^2$, respectively. The fluid is assumed incompressible and irrotational. From the fluid potential $\phi(x,y,z,t)$, the pressure acting on the sheet at $z = \eta$ is defined as

$$p\,(x,y,t) = \rho g\eta + \frac{\partial\phi}{\partial t} + \rho\frac{v^2}{2}, \tag{2}$$

with ρ the fluid density, g the gravitational acceleration, and v the vertical velocity $\frac{\partial\eta}{\partial t}$. The dispersion relation is derived by treating the structural part as a boundary condition. The kinematic boundary condition on the sheet surface is $\frac{\partial\eta}{\partial z} = \frac{\partial\phi}{\partial z}_{z=\eta}$. In the current study the sheet inertia is neglected since $\rho_s \ll \rho$ and deep water is assumed as $\tanh(kH)\approx 1$ for all conditions, with k being the wave number and H the water depth. From equations (1) and (2), the dispersion relation follows as [24, 34]

$$\omega^2 = gk + \frac{T}{\rho}k^3 + \frac{D}{\rho}k^5, \tag{3}$$

with ω the wave radial frequency in rad/s. This relation indicates that deformations are influenced by elastic sheet bending (Dk^5/ρ), elastic deformation due to in-plane tension (Tk^3/ρ) and gravity (gk). Depending on the length scale of the problem and the loads applied on the model, the tension term can either be a uniformly applied pretension [31], a pretension acting on sheet due to the fluid's surface tension [24, 25], or of negligible magnitude [7].

Depending on the length scales of the hydroelastic waves and the fluid and material properties, particular terms in the dispersion relation may contribute very little. The dispersion relation can be simplified accordingly. In the limit of very thin sheets, where the bending rigidity and sheet thickness

approaches zero, the dispersion relation is governed by the air-water surface tension [24]. In fact, the tension term is structurally analogous to the capillary term. In the limit of very long wavelengths, $k \ll (\rho g/D)^{1/4}$, the dispersion relation is governed by the gravity term. The crest velocity, also known as the phase velocity, is defined by

$$c_p = \frac{\omega}{k} = \sqrt{\frac{g}{k} + \frac{T}{\rho}k + \frac{D}{\rho}k^3}. \tag{4}$$

Hydroelastic research on floating membranes typically aims to predict the structural deformations and the subsequent internal loads due to the interplay of the fluid and the structure. The relation between the hydroelastic wavelength and the wave frequency is bound by a dispersion relation, which thus relates space and time. With spatiotemporal analysis, both the wavelengths and the wave frequencies of a system can be computed, leading to a trend between both parameters. The trend found for a particular system can indicate the relevant terms of a dispersion relation, as clearly demonstrated by Domino *et al* [24]. With the experiments in the current study, the dominant terms can be identified through spatiotemporal analysis. This can lead to a justified simplification of the dispersion relation, and thus the momentum balance and structural model.

3. Method

Two experimental setups are used to measure the time resolved deformation of a flexible floating structure. The first setup measures the wave-structure interactions of a $5 \times 1\,\mathrm{m}^2$ floating membrane in a wave tank. The second setup measures accelerating hydroelastic waves generated by a perturbation on a $0.5 \times 0.5\,\mathrm{m}^2$ floating membrane. The following subsections describe the setups, the experimental procedures, and the processing steps. Table 2 presents a summary of the setups, and the processing settings. In the last subsection the measurement uncertainty of both systems is analyzed, while focusing on noise, accuracy, and repeatability.

3.1. Large setup

The large setup uses a DIC setup where the deformation fields of a total of 5 adjacent and synchronized stereoscopic camera pairs are stitched together. This enables the instantaneous measurement of hydroelastic waves over the full $5 \times 1\,\mathrm{m}^2$ domain. Figure 1 presents a schematic impression as well as a picture of the setup.

3.1.1. Experimental setup & model. The experiments are conducted in Towing Tank no. 2 of the Ship Hydromechanics Laboratory at the Delft University of Technology. The tank spans 85 m in length and 2.75 m in width. The water depth H and water temperature are kept constant during the experiment at 1.23 m and 20 °C, respectively. Waves are generated by a piston/flap-type wave maker in piston mode, located 40 m from the measurement location. The other end of the tank has a damping beach to minimize wave reflection. Two wave probes are used to measure the incident wave (WP1), and the hydroelastic waves of the model (WP2), respectively. The locations of the wave probes are indicated in figure 2. WP1 is a wire resistance-based probe that is calibrated daily in steps of 10 mm over a range of 200 mm. WP2 is an ultrasonic wave probe (GeneralAcoustics, Kiel, Germany) and is self-calibrating through an additional probe.

The model is moored in the center of the tank with 4 lines as schematically shown in figure 2. The mooring lines attached to the front corners are very stiff Dyneema lines with a diameter of 0.2 mm and a length of 5 m to avoid stretching due to wave loads. The lines that are attached to the aft corners are lightly prestretched elastic threads with a diameter of 0.5 mm, and are only present to keep the model aligned. The membrane is made of closed-pore neoprene foam, and has an overall length of 5.0 m, width of 1.02 m, and thickness of 0.0048 m. The material density ρ_m is $145\,\mathrm{kg\,m^{-3}}$, and the Young's modulus (E) is 0.83 MPa [35]. These properties are similar to comparable studies, where $E = 2.5$ MPa and $\rho_m = 190\,\mathrm{kg\,m^{-3}}$ [36], and $E = 0.560$ MPa and $\rho_m = 116\,\mathrm{kg\,m^{-3}}$ [7]. Test properties and material parameters are also shown in table 4.

The contrast and the distribution of the speckle pattern on the model strongly influences the measurement resolution and uncertainty. Therefore, a dedicated speckle application method is developed to control these parameters. Speckle stamps of $20 \times 20\,\mathrm{cm}^2$ are designed and 3D printed. The stamps have speckles with a diameter of 7 mm. The spatial variation is optimized by finding a compromise between large blank areas or paint accumulation due to large randomness on one hand, and avoiding a too regular pattern on the other hand. The latter can pose difficulties for image analysis, as subsets can become too similar to be identified from other subsets. Three stamps are used in random order to decrease the repetition of the pattern over the model. The use of predesigned speckle stamps results in a pattern with a uniform speckle density and high contrast.

3.1.2. DIC setup and calibration procedures. The large DIC setup consists of 5 stereoscopic camera pairs that are separated by 1 meter. A front view of the setup is shown in figure 3 The FoV of each stereoscopic camera pair has an overlap of a minimum of 140 px with the FoV of an adjacent pair to ensure their connectivity in the common frame of reference as shown in figure 2. The measurement volume of the large setup consists of a minimal box-shaped domain of 5 meters in length, 1 meter in width and a minimal required depth of 0.18 m, which is the maximum wave height in our wave experiment.

Since the measurement accuracy relies on the calibration of the entire measurement volume [16, 37], a specific calibration procedure is developed. A very stiff LaVision calibration target of $1 \times 1\,\mathrm{m}^2$ is placed on a floater. Then, calibration images are acquired at the mean water level ($H = 1.23$ m) with the target in a horizontal position. A second set of images is acquired with the target at a lowered water level ($H - \eta_{\max}$) in a titled position ($\phi_{\mathrm{tilt}} = \tan^{-1} 2\eta_{\max}/L_{\mathrm{target}}$), to improve the calibration model in the out-of-plane direction.

Table 2. Overview of the DIC equipment and setups, acquisition settings and processing settings.

Category	Parameter	Large setup	Small setup
Cameras	Number of cameras	10	2
	Camera type	SlimX	Photron FASTCAM SA-Z
	Sensors	—	CMOS
	Resolution	1280 px × 1024 px	1024 px × 1024 px
	Exposure time	Not adjustable	0.5 ms
Objectives	Type	5.8 mm	Kreuznach Componon-S 4.0/80 mm
	Extensions	n.a.	Makro-Unifoc 7 (20–28 mm)
	Aperture	Neither specified, nor adjustable	$f/5$
Setup	Stereoscopic angle (2θ)	25 °	14.1 °
	FoV Single stereosc. pair	1750 × 1400 mm^2	290 × 290 mm^2
	FoV Concat. stereosc. pairs	5400 × 1400 mm^2	n.a.
	Scale factor	0.72 px mm^{-1}	3.57 px mm^{-1}
	Speckle size	7 mm	1–2.8 mm
	Water depth	1.23 m	0.45 m
Acquisition	Recording frequency	30 Hz	2000 Hz
	Recording duration	120 s	0.2 s
Processing	Subset size	29 px × 29 px	15 px × 15 px
	Step size	9 px	5 px

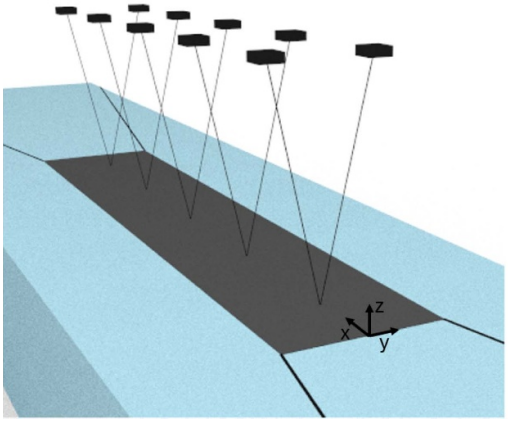

(a) Schematic impression of the large setup with a 5 × 1 m^2 membrane. The deformations of the model are measured with 5 stereoscopic camera pairs, each 1 meter apart. Four mooring lines keep the model in place.

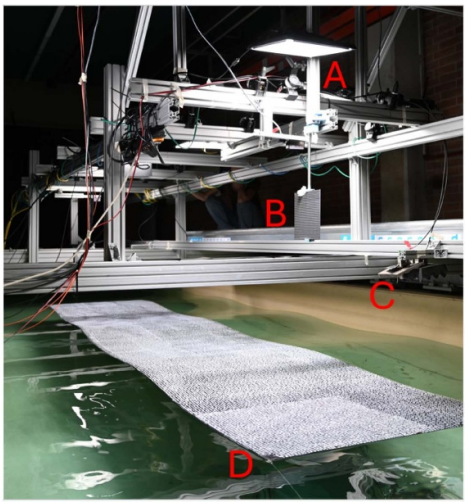

(b) Picture of the large setup. The 10 cameras are mounted on the aluminum profiles. A: LED light, B: PIV calibration target (not used in this study), C: ultrasonic wave probe (WP2), and D: front mooring line tied to the model.

Figure 1. Schematic impression and picture of the large setup.

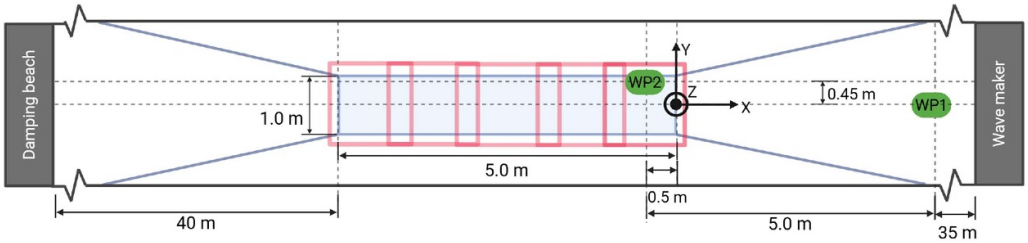

Figure 2. Top view of large experimental setup. The red squares indicate the FoVs of the 5 stereoscopic camera pairs. The FoV closest to the wave maker is referred to as FoV A. WP1 and WP2 refer to the wave probes used in the measurements.

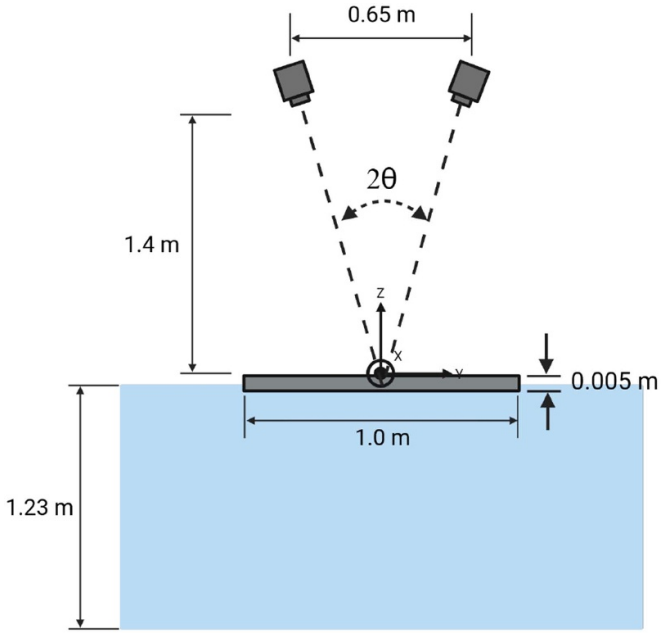

Figure 3. Side view of the large setup for regular wave test. The stereoscopic angle is denoted by $2\theta = 25°$. The channel width is 2.75 m, and is larger than pictured at this image.

Table 3. Incident wave parameters for the regular wave tests in the large setup.

Wave	Amplitude	Period	Wavelength	Steepness	Phase velocity
	η_o [m]	T_o [s]	λ_o [m]	$2\eta_o/\lambda_o$ [-]	c_p [m s^{-1}]
W1	0.03	1.4	3.02	0.02	2.14
W2	0.05	1.0	1.56	0.07	1.60

In this work, the calibration images of individual stereoscopic camera pairs are back-projected in a common frame of reference, such that the deformation fields registered by each image pair can be stitched together to cover the full measurement domain. The relative positions of the camera pairs are registered during the calibration procedure. Therefore, the three marker fiducials (open dots) on the calibration target should be visible in all four cameras of two adjacent stereoscopic camera pairs for at least a few images.

3.1.3. Test conditions for regular hydroelastic waves. Two regular waves with relatively large wave heights are chosen as test conditions, since this study aims to focus on both the spatial resolution and the accuracy during out-of-plane deformations. For these waves, no significant hydroelastic interactions are expected according to the theory in section 2. However, for the specific aims of this study, these waves serve as a good proof of concept, due to their relatively large height. The characteristics of the incident waves are given in table 3. A typical wave envelope of wave W1 is shown in figure 4. The steady state phase of the waves contains approximately 60 wave cycles and is marked by the red rectangle. The wave ramp-up phase is marked by A.

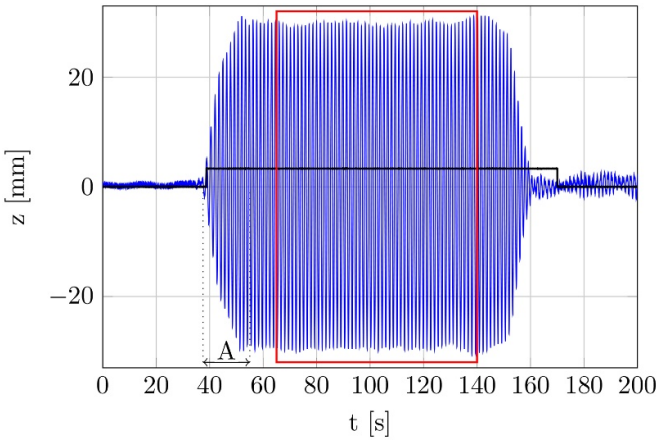

Figure 4. Overview of the wave envelope of wave W1 measured by wave probe WP1. The black line indicates the acquisition period of the DIC images and the red box denotes the steady state phase of the wave envelope. A indicates the ramp-up phase of the wave.

3.1.4. Data acquisition & test procedures. Two computers are dedicated to the data acquisition. The first computer records the signals of the wave probes and the trigger. Before recording at 1000 Hz, these signals are filtered by an analogue low-pass filter with a cutoff frequency at 100 Hz. During the wave tests, a dedicated Arduino device monitors the wave probe closest to the wave maker (WP1). When the wave probe signal exceeds a predetermined threshold in the wave ramp-up phase, a TTL trigger signal is sent to the image acquisition computer to initiate recording. The trigger signal is shown by the black line in figure 4.

The image acquisition computer records the images for the DIC at 30 Hz as compressed JPEG videos with commercial software (Motive version 2.3.4, OptiTrack, NaturalPoint Inc.), dedicated for the OptiTrack cameras. The JPEG compression has a negative effect on the correlation analysis [38]. However, raw images could not be recorded with the current software due to built-in data transfer rate limitations of the software.

Prior to testing, the water level is corrected to its reference level. Air bubbles under the model and water on the model are removed, and the model is realigned when its position is off. To obtain the deformation of the model compared to its undisturbed shape, a reference image in undisturbed water is recorded prior to each test. A minimum waiting time of 30 minutes between successive tests is maintained to minimize any wave disturbances of previous tests.

3.1.5. Processing. The electrical noise of the wave probe and trigger signals is removed using a low-pass filter with a cutoff frequency of 20 Hz. The FIR low-pass filter is designed using the firwin function and applied using the filtfilt zero-phase filter to avoid phase distortion. Both functions are part of the Python scipy.signal library [39, 40]. The data analysis focuses solely on the steady state regime of the waves, marked by the red rectangle in figure 4. To facilitate the analysis, the time axis of the measurements is shifted such that $t = 0$ s corresponds to a zero-upcrossing of wave probe WP2 in the steady

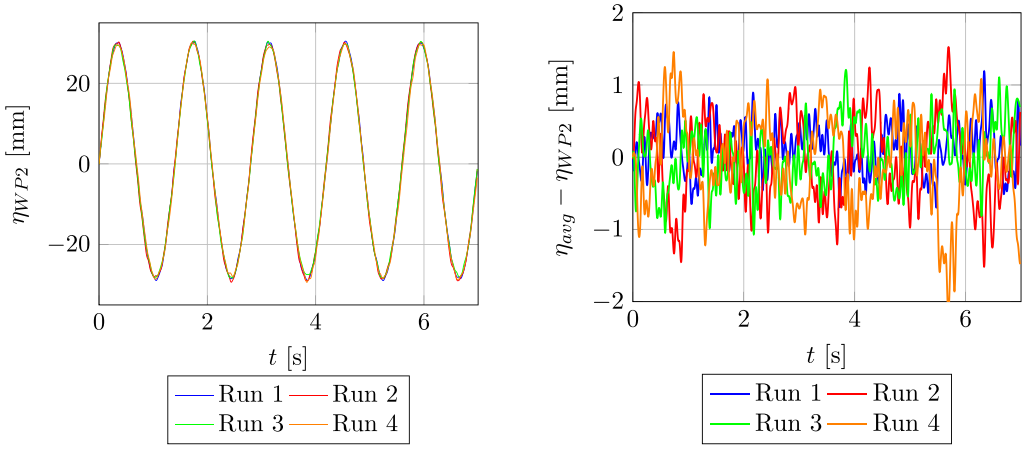

(a) Signal of wave probe WP2 [mm] for four repetitions of wave W1.

(b) Residual amplitude of the WP2 signals.

Figure 5. Repeatability of response of wave W1 in the steady state phase, measured with wave probe WP2. (a) Signal of the wave probe for four repetitions of wave W1. (b) Averaged signal of the four wave probe signals minus the individual wave probe signals. The overall residual amplitude is smaller than 1 mm.

state phase of the wave. Figure 5(a) shows the signals on this adjusted temporal axis.

Figure 5(a) presents the repeatability of the generated waves. Four test repetitions of wave W1 are plotted. The individual responses are subtracted from the average signal, resulting in the residuals plotted in figure 5(b). This graph shows that the overall residual amplitude is smaller than 1 mm, which is also the measurement accuracy of the wave probe.

Prior to DIC processing, TIFF images are extracted from the JPEG videos. Images of the model in undisturbed water are used as reference images. Image processing is conducted with commercial software (DaVis 11 Strainmaster, LaVision GmbH, Göttingen, Germany), using the settings in table 2. The subset size is 29×29 px and the step size is 9 px, therefore resulting in an in-plane spatial resolution of 42 mm and a data spacing of 13 mm. Areas on the images containing structural elements of the experimental setup or wave probes are masked. Figure 6 indicates the region of interest (ROI) of stereoscopic pair 1 and 2, and shows the structural elements limiting the mask. Displacement fields are computed per individual stereoscopic camera pair first, before stitching the five displacement fields to a single domain. Subsets with surface height reconstruction errors larger than 1.0 mm are excluded from the deformation field, since this is above our maximum allowed uncertainty of 1 mm.

3.2. *Small setup*

The small setup consists of a single stereoscopic camera pair and is schematically shown in figures 7(a) and (b). The experiments are performed in the flumetank of the Ship Hydromechanics Laboratory at the Delft University of Technology. The tests are conducted in a water depth of 0.45 m. The square model is made of closed-pore neoprene foam with a density of 124 kg m^{-3}. The Modulus of Elasticity (E) is 1.4 ± 0.4 MPa, computed with a static indention method [7, 41]. The model has an area of 0.50×0.50 m^2 and a thickness of 2.0 mm. The model is kept in position by four elastic thread lines, each line connected to one corner of the model and a sidewall of the tank. The lines have a diameter of 0.5 mm, and no pretension is applied. White speckles with diameters ranging from 1.0 mm (∼3 pixels) to 2.8 mm are applied to this model with a speckle roller, allowing for a relatively constant speckle size.

The cameras are positioned 1 m above the model, and have a stereoscopic angle $2\theta = 14°$. This angle was fixed for this particular setup and is in fact optimized for in-plane accuracy. Enlarging the angle strongly improves the out-of-plane accuracy. An optimal performance for both in-plane and out-of-plane accuracy is reported for stereoscopic angles between 20° and 30° [42]. The stereoscopic camera pair is calibrated with a dot pattern target of 165 mm × 238 mm while the water level is lowered to obtain a measurement volume (0.3 m × 0.3 m × 10 mm) situated around the mean water level. The hydroelastic waves are initiated by a perturbation caused by a steel ball with a mass of 8.3 grams falling onto the membrane. An electromagnet releases the ball and is located 115 cm above the center of the model. This perturbation yields a high repetition accuracy due to the constant release height. Before testing, air bubbles and water on the model are carefully removed, and the zoomed-in live images of the cameras are examined to prevent the occurrence of wave disturbances of the previous test.

The image acquisition is controlled by commercial software (Photron FASTCAM Viewer 4, Photron Ltd Tokyo, Japan) and the recording is initiated by a TTL trigger, which is sent when the electromagnet releases the steel ball. The steel ball impacts the sheet with ≈ 5 m s^{-1}. The recording frame rate is set to 2 kHz such that the deformation after impact is captured with a minimum length scale of 10 mm. The duration of the recording is 0.2 s to capture the full traveling wave, as characterized by the maximum phase velocity of ≈ 2 m s^{-1}

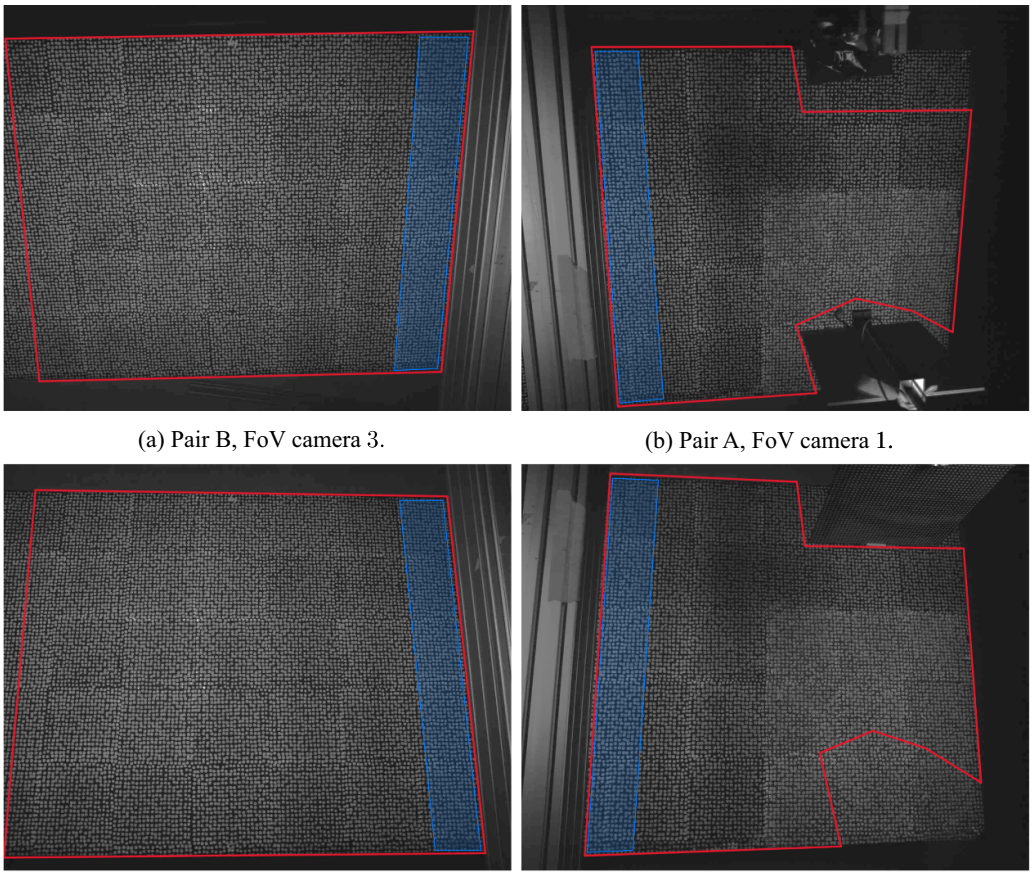

(a) Pair B, FoV camera 3.

(b) Pair A, FoV camera 1.

(c) Pair B, FoV camera 4.

(d) Pair A, FoV camera 2.

Figure 6. Raw images and regions of interest (ROI) of camera 1, 2, 3, and 4, composing stereoscopic pair A (front pair) and B (second pair). The overlapping regions of pair A and B are displayed in blue.

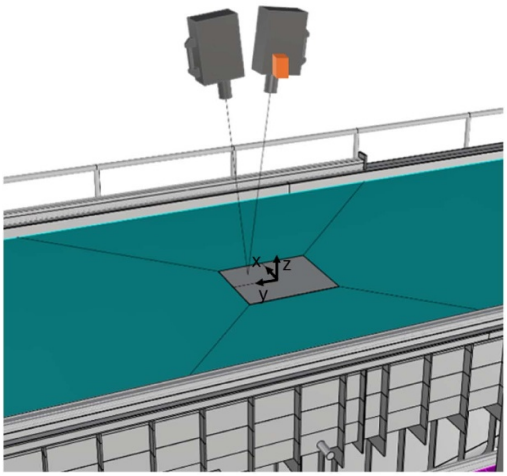

(a) Schematic impression of the small setup with a 0.5 × 0.5 m^2 membrane. The electromagnet is indicated by the orange box, and positioned 1.15 m above the center of the model. Four mooring lines keep the model in place. Drawing by Peter Poot and Pascal Taudin Chabot (2023).

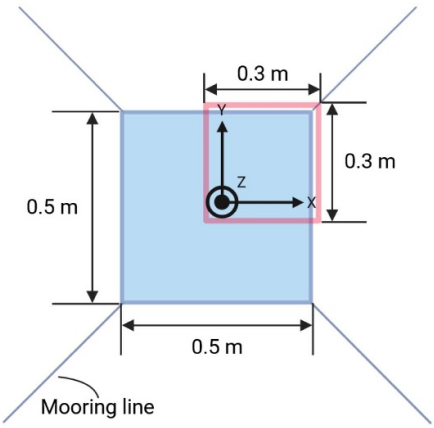

(b) Top view of the small setup, consisting of a single stereoscopic camera pair. The red square represents the FoV. The origin of the coordinate system is at the center of the model.

Figure 7. Small setup. (a) 3D drawing. Adapted with permission from Peter Poot and Pascal Taudin Chabot, TU Delft, and (b) top view of the small setup.

Table 4. Parameters and properties.

		Large setup	Small setup
σ		73 Nm^{-1}	73 Nm^{-1}
ρ		1000 $\mathrm{kg\,m}^{-3}$	1000 $\mathrm{kg\,m}^{-3}$
ρ_m		145 $\mathrm{kg\,m}^{-3}$	124 $\mathrm{kg\,m}^{-3}$
ν		0.4	0.4
h		0.0048 m	0.0020 m
E		0.83 MPa	1.4 MPa
D	$\frac{Eh^3}{12(1-\nu^2)}$	$0.91{\cdot}10^{-2}$ Nm	$1.1{\cdot}10^{-3}$ Nm
λ_{cap}	$2\pi\left(\frac{\sigma}{\rho g}\right)^{1/2}$	0.017 m	0.017 m
λ_c	$2\pi\left(\frac{D}{\rho g}\right)^{1/4}$	0.20 m	0.12 m

(equation (4)) and the domain length of 0.25 m. Material properties and test parameters are shown in table 4.

Images are processed with open source DIC software (DIC Engine, or DICe [43]). Since this software is designed for in-plane strain, the DIC processing could only be performed with limited stereoscopic angles, here set to $2\theta = 14°$. All processing is done with respect to the coordinate system defined in figure 7(b). The center of impact is manually selected as the origin of the coordinate system, such that shifting of the center of impact due to small drift effects are compensated prior to processing. The specifications and settings of the setup and cameras, as well as the processing settings are given in table 2.

3.3. Uncertainty assessment

The measurement errors in DIC experiments are composed of noise and bias errors. In the current study the out-of-plane accuracy is of major interest since the focus is on transverse hydroelastic waves. The accuracy should thereby be homogeneous over the entire domain, such that the response at different locations on the membrane can be compared. Both noise and bias errors in the planar domain are addressed in the following subsections, as both types can contribute to the out-of-plane uncertainty [17].

3.3.1. Noise. The noise for each quantity of interest is often quantified with the spatial and/or temporal standard deviation [44] of a measurement of the quiescent model. These metrics indicate the minimum noise levels or *noise floor*. This is generally associated with the hardware, the contrast, the lighting, the exposure time, and the processing algorithms [44]. In the current setups noise could be imposed by low and high frequency water waves, air movements, vibrations in the camera support structure, and compressed image sizes. To identify possible low frequency noise such as standing waves, the quiescent model is measured for a duration equal to the maximum relevant duration of the hydroelastic wave test. This is 7 s for for the large setup, composed of 5 cycles of a 1.4 s wave period. The maximum test duration of the small setup is 0.2 s. The results for the noise floor are 0.03 mm for the displacement x, 0.06 mm for the displacement in y, and 0.09 mm for the displacement in z direction for the large setup. For the small setup the noise floor is 0.03 mm in z direction.

3.3.2. Bias. The bias in the out-of-plane direction is evaluated for the large setup by comparing the DIC results with a reference measurement with ultrasonic WP2. For this test, the water level is lowered in steps of 10 mm, and images and wave probe data are recorded at each step. The DIC displacement is defined by the average out-of-plane displacement of all subsets of FoV A, and is compared with the wave probe signal, see figure 8. The inset shows the residual between both measurements, and indicates that the bias error does not increase for increasing displacement. The wave probe accuracy is <1 mm according to the manufacturer's statement. The inset shows that the residual displacement is less than 1 mm, so that the bias error of the DIC system falls within the uncertainty range of the wave probe and is thus less than 1 mm for the whole measurement depth.

A second indication of a possible bias error is the stereo reconstruction error, which is computed from the calibration. For the large setup this is 0.1 px ($\sim$0.1 mm), which clearly falls within the 1 mm range. For the small setup this is also 0.1 px.

3.3.3. Planar uncertainty. The surface height reconstruction error describes the deviation between a point on the original image and the back projection of a reconstructed 3D point onto the original image. It therefore serves as a measure of the calibration quality. On the other hand, a low image contrast increases the error as well, since significant grey-scale intensity differences are more difficult to distinguish. Figure 9(a) shows the surface height reconstruction error over the planar domain of stereoscopic camera pair A. Here, the mean error is 0.33 mm, and the standard deviation is 0.045 mm. The error hardly increases towards the edges of the model, indicating a proper correction of the camera distortion. This particular result is important for spatiotemporal analysis over the domain, since this requires a reliable comparison between different locations in the domain. The error in the upper left corner is significantly larger. Here, the lower light intensity causes a poorer contrast and thus less distinguishable grey-scale intensities, which most likely results in the observed error increase. The planar uncertainty however remains less than 1 mm for the entire FoV, as figure 9(a) shows.

Figure 10 presents the surface height reconstruction error of the 5 stitched stereoscopic camera pairs for the model in quiescent conditions. The figure clearly shows that the error ranges from 0.2 mm to about 0.4 mm along the length of the model with little variation over the width. There are two distinct regions where the error increases to 0.6 mm, which is around $x\approx -2.0$ m and $x\approx -4.0$ m. This systematic error is a result of the calibration procedure. The calibrations of each stereoscopic camera pair are projected onto a common frame of reference with only a few dots that are visible in all four cameras of adjacent pairs. Inaccuracies in resolving the precise rotation of the calibration target at one edge of the FoV can result in relatively large errors at the opposite edge of the FoV. By taking a closer look at the figure, a gradual increase of the surface height reconstruction error can be observed from for example $x\approx 1.0$ m to $x\approx 2.0$ m, indicating an unwanted tilt.

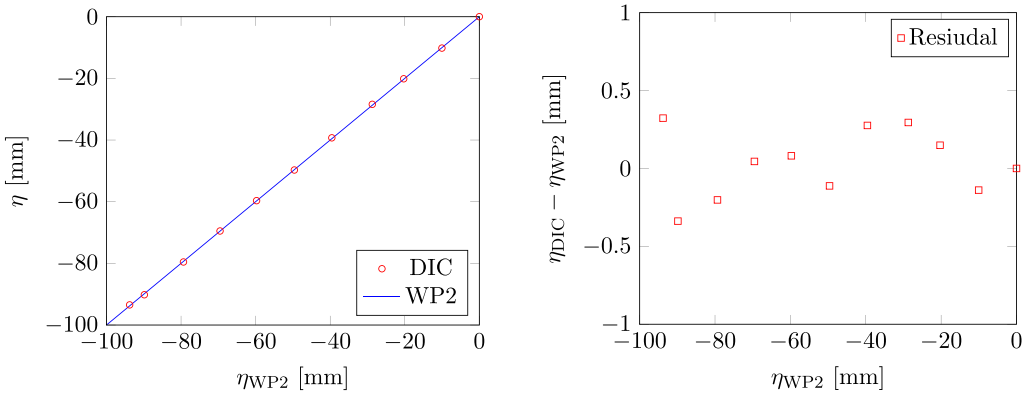

(a) Amplitude of displacement. (b) Residual displacement.

Figure 8. Out-of-plane displacement of the model as measured by the DIC system (average displacement of the FoV of stereoscopic camera pair A) compared to displacements measured with WP2. (a) Direct comparison. (b) Residual displacement ($\eta_{DIC} - \eta_{WP2}$).

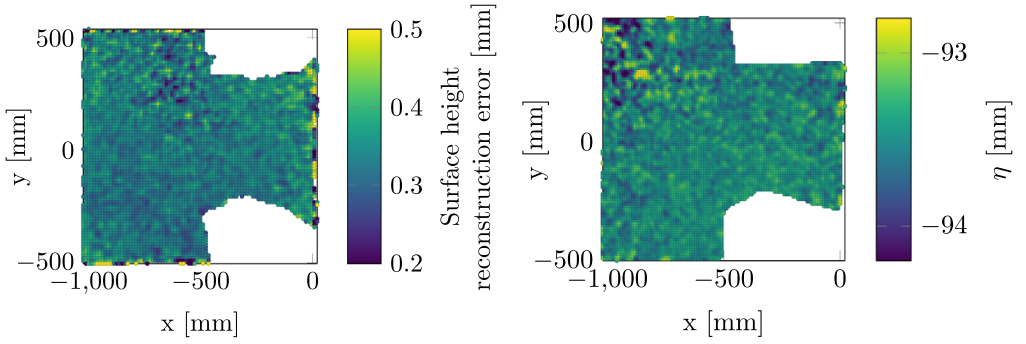

(a) Surface height reconstruction error of stereoscopic camera pair A, closest to the wave maker. (b) Out-of-plane displacement η with the water level decreased to z = -93.0 ± 0.6 mm.

Figure 9. Surface height reconstruction error and out-of-plane displacement over planar domain of FoV A of the large setup, which is the FoV closed to the wave maker. The odd-sized shape is a result of masked regions due to equipment blocking the camera views.

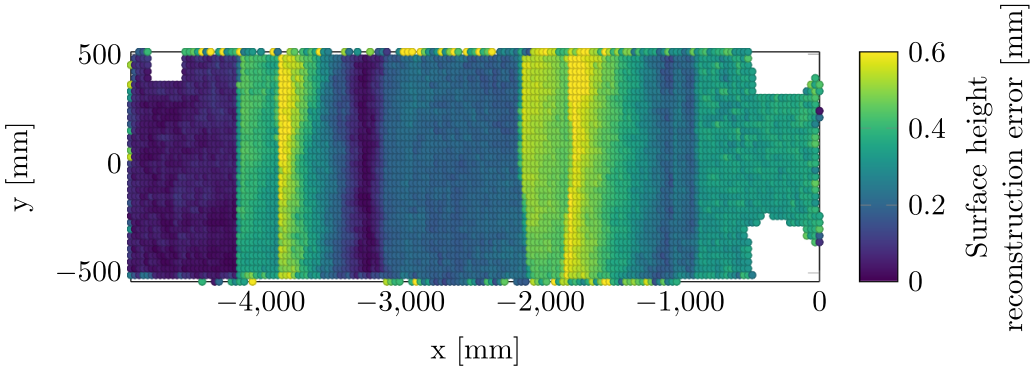

Figure 10. Surface height reconstruction error of stitched stereoscopic camera pairs.

4. Results and discussion

4.1. Large setup: regular wave excitation

The large test setup measures the displacements of the membrane in regular wave excitation from the piston-flap wave maker. The instantaneous membrane deformation for wave W2 is shown in figure 11. The membrane follows both incident waves W1 and W2 closely. Little wave radiation and wave diffraction are observed during the experiments, and there is no significant overwash that disturbs the quality of the measurements or affects the stereoscopic correspondence.

4.1.1. Accuracy in regular waves. The accuracy of the DIC setup is compared with a reference measurement system, WP2. The phases of both signals are matched by correlation, since the location with respect to the DIC coordinate system is

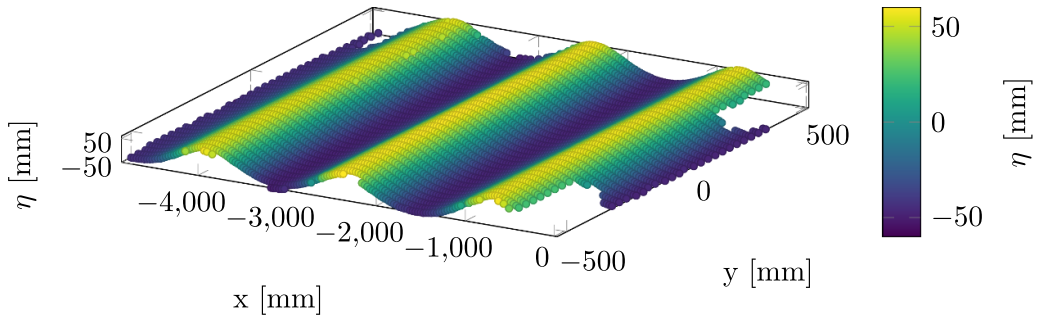

Figure 11. 3D surface view of membrane deformation for W2. The wave direction is from right to left.

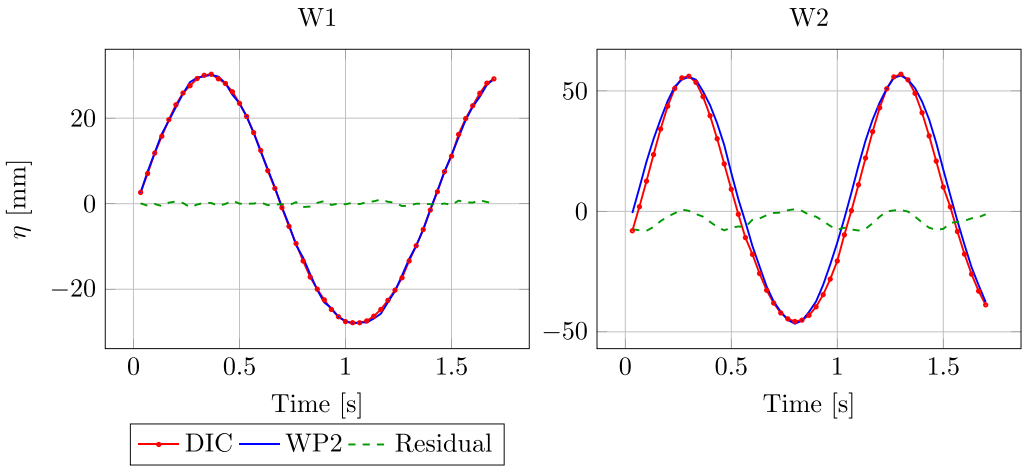

Figure 12. Comparison of DIC and WP2. The residual between the DIC signal and the wave probe signal has a mean value of 0.1 mm and −3.53 mm and a standard deviation of 0.54 mm and 2.8 mm for W1 and W2, respectively. The the residual at the troughs and crests is sub-millimeter, and the largest signal deviations occur at the slopes.

not exactly known. Figure 12 shows the wave envelopes of both wave cases. For W1, both signals closely follow each other. The mean of the residual amplitude is 0.00 mm, and its standard deviation is 0.55 mm. The mean signal difference at the troughs and crests is 0.51 mm. The signals show larger discrepancies for W2. Although the mean signal difference of the troughs and crests is 0.22 mm with standard deviation 0.41 mm, which remains well below the ultrasonic wave probe accuracy of 1 mm, significant offsets are visible at the slopes of the wave. The time-trace as plotted in figure 12 is extracted for each time step by finding the closest data point with respect to the expected location of the WP, including the surge and sway motions. The grid spacing of 12.5 mm can induce a vertical error of 0.8 mm or 2.5 mm for W1 and W2, respectively, which is directly influenced by the slope, and thus the wave steepness.

4.1.2. Spatiotemporal analysis. The instantaneous membrane deformations during wave loads W1 and W2 are shown in figure 13. A spatiotemporal analysis of the membrane deformations is conducted with the current setup. From theory we know that in open water with a wavelength significantly longer than the gravity-capillary wavelength of ≈ 1.7 cm ($\lambda_{cap} = 2\pi\sqrt{\sigma/\rho g}$) [24], the gravity term is the only governing parameter in the dispersion relation, reducing equation (3) to $\omega^2 = kg$ for deep water with $\tanh(kH)\approx 1$. The bending rigidity term in equation (3), $k^5\frac{D}{\rho}$, should be substantial in relation to the gravity term kg to notice a considerable change in the wavelength with the presence of the membrane. For both wave conditions, the theoretical magnitude of these terms is included in table 5. Therefore, $k^5\frac{D}{\rho} \ll gk$ for both cases, and no significant influence of the bending term is expected.

Figure 14 shows the propagation of the crests through the membrane over time in the propagation direction x. The propagation is plotted through three longitudinal slices along the x-axis: at $y = -450$ mm, 0 mm, and 450 mm, respectively. The linear trend indicates a constant crest velocity, which is expected for regular waves. From the figure, the phase velocities are determined as $2.13\,\mathrm{m\,s^{-1}}$ for W1 and $1.60\,\mathrm{m\,s^{-1}}$ for W2. With equation (4) and $\lambda = 2\pi/k$, the hydroelastic wavelengths are computed, resulting in 2.91 ± 0.01 m and 1.64 ± 0.004 m for W1 and W2. The theoretical wavelengths are 3.02 m and 1.56 m, respectively. Therefore, wave modulation (i.e. wave lengthening and shortening) of −0.1 m and +0.08 m is found, respectively. This shows a slight discrepancy between the theory of using the dispersion relation as wavelength predictor, and indicates that other parameters, such as the mass of the membrane [46] or the wave steepness [47] influence the modulation as well.

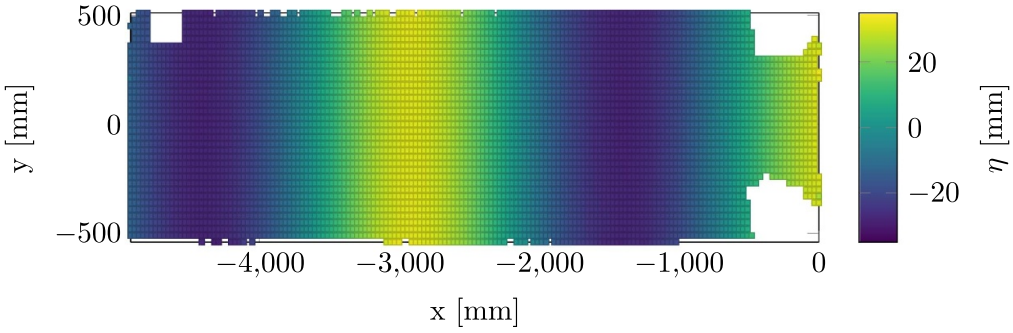

(a) W1: Instantaneous membrane deformation η.

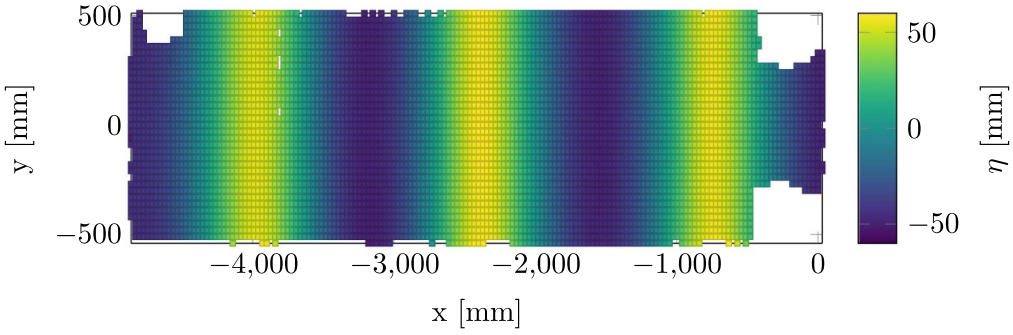

(b) W2: Instantaneous membrane deformation η.

Figure 13. Instantaneous membrane deformation η [mm] for W1 and W2. The blank areas are masked due to equipment in the FoVs of the stereoscopic camera pairs. The data is openly available [45].

Table 5. Theoretical magnitude of dispersion relation terms.

	kg	$k^5 \frac{D}{\rho}$
W1	20.4 rad s^{-2}	4.00·10^{-4} rad s^{-2}
W2	39.5 rad s^{-2}	1.09·10^{-2} rad s^{-2}

Secondly, figure 14 shows that the crests of the three different slices propagate with equal phase velocities. This indicates that no notable change in wavelength occurs over the width of the membrane. Wave modulation is reported by Sree *et al* [8], which they linked quantitatively to the viscoelastic properties of the floating sheet. Therefore, in the current experiment, viscoelastic effects are probably negligible. Also, these modulations in a continuous 3D system like in our current setup, could lead to differences in wave modulation over the width of the model since the continuity of the water body should be satisfied.

4.2. Small setup: hydroelastic waves by an impact

4.2.1. Accuracy during static indention. A simple indention experiment is conducted to analyze the effect of bias, repeatability and noise during an out-of-plane DIC test. A point load is applied in seven steps of 0.022 N in the center of the model. Figure 15 shows the displacement of two load steps, in which each step shows four repetitions. Fourth order polynomial trend lines are fitted through the data of each repetition.

First, the standard deviation of the noise around the trend lines is 0.05 mm (∼0.2 px). Second, figure 15(a) indicates a very repeatable test. However, the trend lines in figure 15(b) show a varying offset from $z = 0$. This offset is a clear bias error since it is the computed height with respect to the reference image. Its maximum magnitude is 0.2 mm (∼0.7 px) and its standard deviation is 0.073 mm over four repetitions of (∼1.8% of the maximum displacement). Despite this offset, the trend line curves remain nearly identical. The load step 0.154 N yields the largest bias error of all load steps. A comparable experiment on free surface displacement reported a vertical error of 1 mm [48] for a similar sized domain. The current bias error of 0.2 mm thus shows more accurate results.

During wave-structure interaction tests, the deformation shape and peak-through magnitude (i.e. the wave height) is often the primary focus. Therefore, an initial offset would not necessarily cause a deteriorating accuracy for the required output, since the shapes of the trend lines yield the most relevant information. This combined test thus shows that the deformation shapes are repeatable and accurately retrieved. The largest error here is the bias error of 0.2 mm (0.7 px, or 4% of the maximum vertical displacement). The standard deviation of the noise has a very acceptable level of 1.25 % of the maximum vertical displacement. The bias error

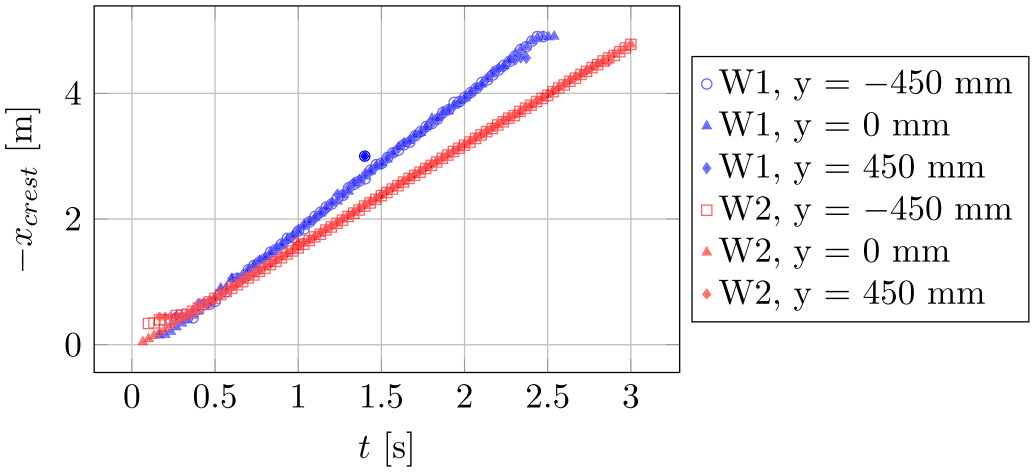

Figure 14. Crest propagation of W1 and W2. As derived from this figure, the crest velocities are 2.13 ± 0.010 m s^{-1} and 1.60 ± 0.004 m s^{-1}, respectively. For each wave condition, the membrane deformations at three slices along the -x-axis are plotted.

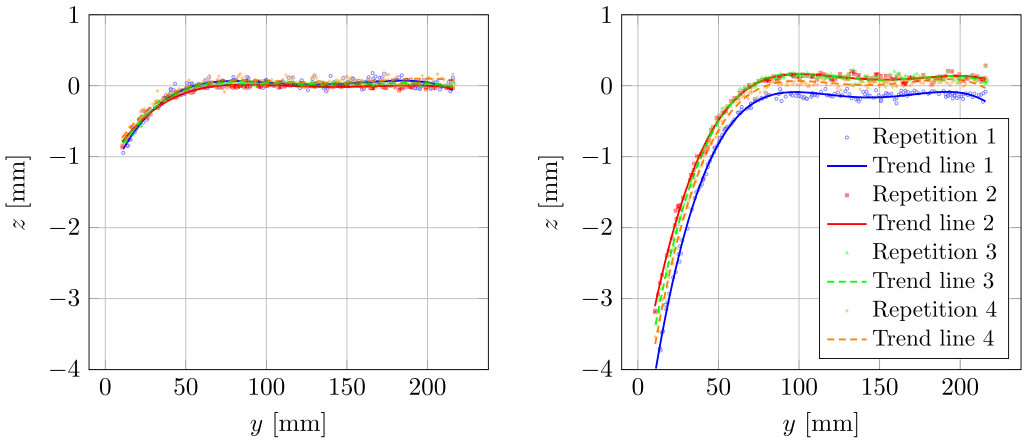

(a) Static indention with point load $P = 0.022$ N

(b) Static indention with point load $P = 0.154$ N. The offset from $z = 0$ is the largest for this test and is therefore included.

Figure 15. Vertical displacements along the radial line $x = 0$ during static indention tests, each repetition fitted with fourth order polynomial trend lines. The point load is applied at $y = 0$ mm. The deflection reaches the mean water level again 60 to 80 mm from the center. Each graph shows data and trend lines of four repetitions.

does not increase towards the edge of the domain. Therefore, this method is suitable for large spatial domains, and has a maximum out-of-plane error of 0.2 mm, which is a subpixel accuracy.

4.2.2. Accuracy during impact test. The aim of the small test setup is to measure unsteady hydroelastic waves, and assesses the repeatability of the measurement system with a highly repetitive perturbation from the impact of a steel ball. For this test, the fluid and membrane are initially at rest. The impact occurs at $t = 0$ s, thereafter, the ball looses contact at $t = 0.026$ s when it bounces off until it impacts the membrane again at $t = 0.164$ s. Displacements of the membrane and fluid occur within microseconds after the first impact. Figure 16 shows the vertical displacement of the membrane at $t = 0.051$ s and $t = 0.126$ s. Figure 17(a) presents several time instances of the hydroelastic wave along the radial line of $y = 0$ mm. A wave with a steepness of $\frac{\Delta z}{\Delta x} = 0.4$ is initiated right after the impact shown at $t = 0.013$ s. Apart from this main perturbation, several smaller ripples are visible to the right of the first, i.e. largest, crest. With progressing time, the steep wave and ripples propagate towards the edges of the membrane.

Figure 17(b) shows spline fits of the hydroelastic wave for four repetitions of the measurement. The splines are fitted with the UnivariateSpline function of Pythons SciPy package [39, 40], with a fit smoothing factor (s) set to 0.2, balancing between closeness to individual data points and smoothness. Figure 17(a) shows both the data and the spline fit. The standard deviation of the crest height and planar location of crest 1 over the five repetitions is 1.3 mm in x (∼4 px) and only 0.04 mm in z (∼0.1 px), which is 0.6% of the spatial domain and 1% of the wave amplitude. Ripples can be distinguished from a minimum amplitude of 0.15 mm (∼0.5 px). The repetitions do not deviate significantly from the mean water level.

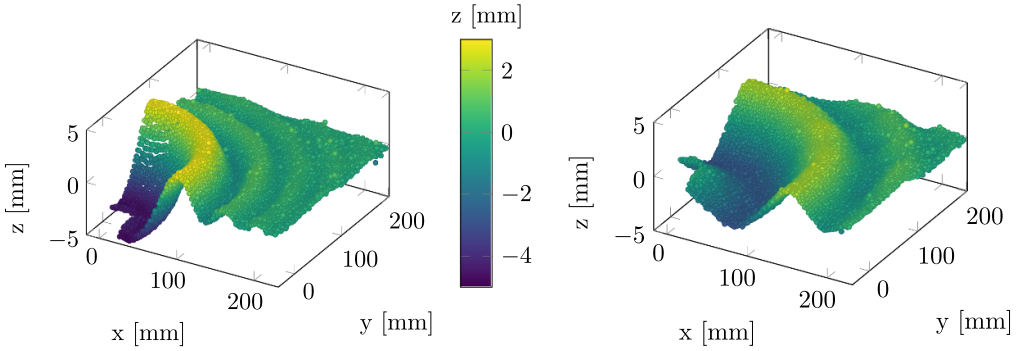

(a) Vertical membrane displacement at 0.051 s after impact.

(b) Vertical membrane displacement at 0.126 s after impact

Figure 16. Hydroelastic wave radiation after the steel ball impact at $(x, y) = (0, 0)$ mm at $t = 0$ s. The graph shows a quarter of the membrane. The waves propagate towards the positive x- and y-axis. The data is openly available [45].

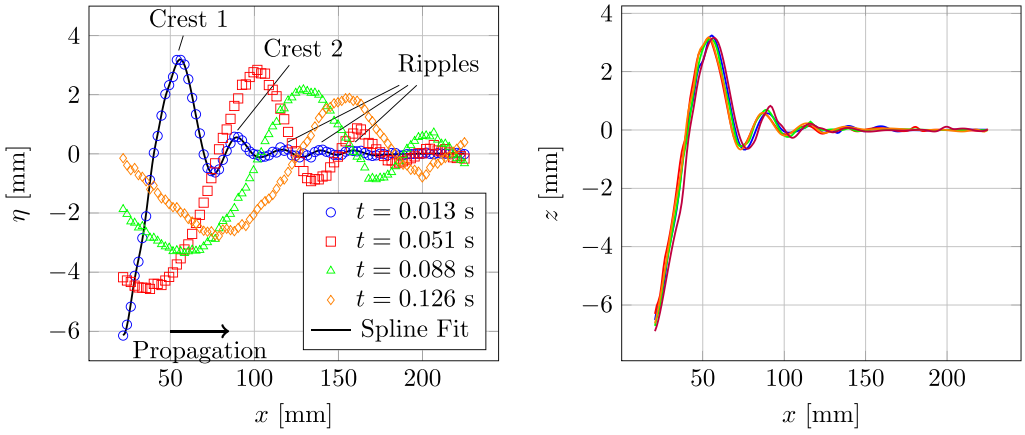

(a) Hydroelastic wave envelope along radial line $y = 0$ mm. The annotations refer the blue data points.

(b) Spline fits of the hydroelastic wave amplitude of 4 repetitions along radial line $y = 0$ mm at $t = 0.013$ s.

Figure 17. Hydroelastic waves along the radial line $y = 0$. (a) Crest 1 decreases in amplitude and steepness over time and propagate towards the edge of the membrane. (b) Spline fits with $s = 0.2$ of the vertical membrane deformation, showing the steep initial wave and multiple ripples towards the positive x-axis. The repetitions are in close agreement and ripples can be distinguished from a minimum amplitude of 0.15 mm.

In terms of repetition uncertainty, the current study performs similar to other studies. For instance, Wu *et al* [49] used stereoscopic DIC to measure the free surface water dynamics with a surface height change of 7 mm. The maximum difference in amplitude between the repetitions was 0.41 mm, which corresponds to an error of 6% of the domain height. Schreier and Jacobi [7] conducted stereoscopic DIC on a floating thin elastic sheet, achieving a vertical repeatability of 0.5 mm (∼0.7 px) for wave amplitudes of 10 and 20 mm. The repetition accuracy achieved here is thus similar to that of reference studies.

4.2.3. Spatiotemporal analysis. The amplitude of the crest closest to the perturbation (crest 1) linearly decreases within a time interval $0.01 < t < 0.2$ s. The amplitude of the wave next to the main perturbation wave (crest 2) remains constant within this time interval. Figure 18(a) shows the propagation of both crests. They follow a clear trend that appears to scale with $t^{0.44}$. The measured deformation shown in figure 17(a) corresponds well with numerical results obtained by O'Kiely *et al* [50]. That study also finds an initial steep wave and outward propagating ripples. Experimental results are obtained as well, although for floating membranes with a thickness much smaller than the maximum deformation amplitude [51, 52]. Those membranes clearly fall in the response regime in which the bending rigidity has minimal influence. As a result, the deformation after impact is less smooth, and includes wrinkle formation. On the other hand, the absence of wrinkle formation in the current experiment indicates a notable influence of the bending rigidity. The study by Duchemin and Vandenberghe [51] shows that the position of the wave front scales with $\sim t^{2/3}$. This is a scaling law reported by Keller and Miksis [53] for surface tension-driven flows, which thus also applies for thin floating membranes. The difference between $\sim t^{2/3}$ and the current relation $\sim t^{0.44}$ clearly shows that the present thicker membrane does not behave similar to surface

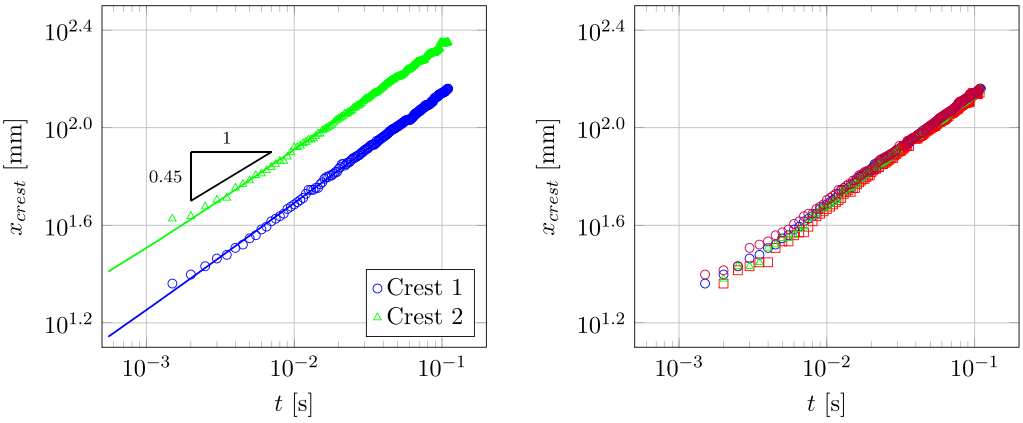

(a) Propagation of crest 1 and crest 2.

(b) Propagation of crest 1 for 4 repetitions.

Figure 18. Propagation of the wave front. (a) Log-log plot. The propagation of crest 1 (○) and crest 2 (△) scale almost equally, with $x_{\text{crest}} \sim t^{0.45}$ for ○ and $x_{\text{crest}} \sim t^{0.44}$ for △. (b) Log-log plot of the position crest 1 for 4 repetitions. The repetitions show a slight offset in x_{crest} but indicate an equal velocity.

tension-driven flows, and that the membrane properties (e.g. bending rigidity, thickness) thus alter the dynamic membrane deformation.

4.3. Scalability and application

The results of the current study show that stereoscopic DIC can both capture the global and detailed deformations of a structure. Those details can for instance be ripples and ripple growth, as shown during the perturbation experiment, but can also be three-dimensional phenomena such as localized wrinkling or spatially varying attenuation. Since global deformations can well be captured with less advanced methods, this method especially proves its benefits for detailed deformations. Although not the case in the current experiments, water on the model can cause reflections and subsequent correspondence problems between stereoscopic cameras. A layer of water on the model could induce an additional error source due to refraction. Compensating for refraction is a possibility for further work.

The two setups in this paper indicate a high level of scalability of the measurements. Although this paper focuses on laboratory scale experiments, this setup could readily be adjusted for real scale applications, similar to the LiDAR setup used by Martins *et al* [23], who measured waves in the coastal zone from a pier. The setup dimensions of a single stereoscopic pair can be scaled linearly, while maintaining a constant stereoscopic angle. By scaling with a factor 10, the system may measure wave heights up to 1–2 m in a spatial domain size of 10 m by 10 m for a single stereoscopic pair. Since the method is 3D, the spatial resolution is the main limiting factor in measuring complex and irregular wave fields. The current experiment shows the systems ability to accurately retrieve high waves, since wave heights of 10% of the domain width could be retrieved with a sub-millimeter accuracy. However, correlation algorithms rely on the presence of features, which can be painted speckles or naturally occurring features on an object. Real scale applications would require either naturally occurring features or should be prepared with recognizable features. The contrast of the features may influence the quality of the measurement, and the distribution may influence the viable spatial resolution [54, 55].

5. Conclusions

This study demonstrates the suitability of multicamera stereoscopic DIC for hydroelastic research of floating membranes in waves. While previous studies could only capture parts of the model, the current study presents a method to apply multicamera stereoscopic DIC in a large domain to obtain deformation data of the entire model. The current side-by-side stereoscopic setup of 10 cameras covers the large domain of 5.0 m × 1.0 m × 0.2 m, while achieving an uncertainty that remains smaller than the equivalent size of a pixel over this entire domain. Wave heights up to 100 mm are measured with a sub-millimeter accuracy. We propose a repeatable calibration procedure for large 3D domains, and designed and manufactured speckle stamps for optimal speckle application on the model. Compared to a speckle roller, speckle stamps are recommended, since the use of the speckle roller resulted in less uniform speckles and a lower contrast than achieved with the speckle stamps used previously in the large setup. The current method to project the calibrations of the individual stereoscopic camera pairs onto a common frame of reference poses limitations, which increased the bias error over the domain. Presumably, post calibration corrections, larger overlapping FoVs, or an adjusted procedure could decrease these effects.

The spatiotemporal analysis of the large setup shows that for the current membrane and test conditions, the equation for the phase velocity (equation (4)) could be simplified by the open water dispersion relation for gravity waves; a conclusion that coincides with theory. The impact test at the small setup shows that the dispersion relation can neither be simplified to pure gravity dominated waves nor to surface-tension dominated waves. Further more, we observe that the hydroelastic phase after a perturbation increases over time by a power law. Its magnitude deviates from studies with

much thinner membranes, which indicates the relevance of the bending rigidity for the current, thicker membrane. The results obtained by this spatiotemporal analysis of unsteady hydroelastic interactions indicate its potential use for the derivation of dynamic scaling laws. Further investigations on the scaling law are planned for the near future, since these laws are necessary for future research on the expanding field of flexible floating structures in gravity waves.

As far as we are aware, this is the first study that presents a full domain analysis of a large, floating structure of size $O(10^1\ \mathrm{m})$ through side-by-side stereoscopic DIC, and also justifies its use by a thorough uncertainty analysis. This work can serve as a foundation for further development and application of stereoscopic DIC for such structures. It is expected that this full-field method will contribute to questions about the fluid-structure interactions of floating membranes in waves.

Data availability statement

The data that support the findings of this study are openly available at the following URL/DOI: https://doi.org/10.4121/3a3f5341-5d75-4caa-96c5-c3f07530f9a5.

Acknowledgments

This study was funded by the Dutch Research Council (NWO) under the Grant Number 19002 ('FlexFloat')in the Open Technology Program (OTP). The authors are grateful for the collaboration with E Uksul, and the technical support by C P Poot, J G den Ouden, S Tokgöz, F J Sterk, P Taudin Chabot and A Piras.

Author contributions

Hanna Pot 0009-0006-6275-7721
Conceptualization (equal), Formal analysis (lead), Investigation (lead), Methodology (lead), Visualization (lead), Writing – original draft (lead), Validation (lead)

Jerry Westerweel 0000-0002-2799-5242
Funding acquisition (supporting), Methodology (equal), Supervision (equal), Writing – review & editing (equal)

Sebastian Schreier 0000-0001-6368-8154
Conceptualization (equal), Funding acquisition (lead), Methodology (equal), Project administration (lead), Supervision (equal), Validation (equal), Writing – review & editing (equal)

References

[1] Cho I H and Kim M H 1998 Interactions of a horizontal flexible membrane with oblique incident waves *J. Fluid Mech.* **367** 139–61
[2] Trapani K, Millar D L and Smith H C M 2013 Novel offshore application of photovoltaics in comparison to conventional marine renewable energy technologies *Renew. Energy* **50** 879–88
[3] Claus R and López M 2022 Key issues in the design of floating photovoltaic structures for the marine environment *Renew. Sustain. Energy Rev.* **164** 112502
[4] Vernet M and Falcon E 2025 Thermodynamics and statistical equilibrium of large-scale hydroelastic wave turbulence *Phys. Rev. Lett.* **135** 024004
[5] Dhote B, Moisy F and Herreman W 2025 Flexible floaters align with the direction of wave propagation *Phys. Rev. Fluids* **10** 074801
[6] Agarwal S, Colomés O and Metrikine A V 2024 Dynamic analysis of viscoelastic floating membranes using monolithic finite element method *J. Fluids Struct.* **129** 104167
[7] Schreier S and Jacobi G 2021 Experimental investigation of wave interaction with a thin floating sheet *Int. J. Offshore Polar Eng.* **31** 435–44
[8] Sree D K K, Law A W K and Shen H H 2017 An experimental study on the interactions between surface waves and floating viscoelastic covers *Wave Motion* **70** 195–208
[9] Montiel F, Bonnefoy F, Ferrant P, Bennetts L G, Squire V A and Marsault P 2013 Hydroelastic response of floating elastic discs to regular waves part 1: wave basin experiments *J. Fluid Mech.* **723** 604–28
[10] Meylan M, Bennetts L, Cavaliere C, Alberello A and Toffoli A 2015 Experimental and theoretical models of wave-induced flexure of a sea ice floe *Phys. Fluids* **27** 041704
[11] Yoon J S, Cho S P, Jiwinangun R G and Lee P S 2014 Hydroelastic analysis of floating plates with multiple hinge connections in regular waves *Mar. Struct.* **36** 65–87
[12] Michele S, Zheng S, Buriani F, Borthwick A G L and Greaves D M 2023 Floating hydroelastic circular plate in regular and irregular waves *Eur. J. Mech. B* **99** 148–62
[13] Orphin J, Fleming A and Algie C 2017 Physical scale model testing of a flexible membrane wave energy converter: videogrammetric analysis of membrane operation *Int. J. Mar. Energy* **20** 135–50
[14] Kristiansen T, Gron P and Faltinsen O M 2022 A floating membrane solar island study *Proc. 9th Int. Conf. Hydroelasticity Mar. Technol.* pp 445–54
[15] Pambela A R, Ma C, Maeda T and Iijima K 2023 Stokes wave traveling along a thin elastic plate floating at water surface *J. Fluids Struct.* **120** 103919
[16] Gomit G, Chatellier L and David L 2022 Free-surface flow measurements by non-intrusive methods: a survey *Exp. Fluids* **63** 94
[17] Sicard J and Sirohi J 2013 Measurement of the deformation of an extremely flexible rotor blade using digital image correlation *Meas. Sci. Technol.* **24** 065203
[18] Wang K, Cheng B, Li D and Xiang S 2024 A speckle projection-based 3D digital image correlation method for measuring dynamic liquid surfaces *Exp. Fluids* **65** 168
[19] Pan B 2018 Digital image correlation for surface deformation measurement: historical developments, recent advances and future goals *Meas. Sci. Technol.* **29** 082001
[20] Streicher M, Hofland B and Lindenbergh R C 2013 Laser ranging for monitoring water waves in the new deltares delta flume *ISPRS Ann. Photogramm. Remote Sens. Spatial Inf. Sci.* **2** 271–6
[21] Zhang L, Shi J, Zhu Y, Zhang C, Zhang Z and Zheng J 2023 An experimental study on monitoring wave profiles with LiDAR *Ocean Eng.* **285** 115436
[22] Blenkinsopp C E, Turner I L, Allis M J, Peirson W L and Garden L E 2012 Application of LiDAR technology for

measurement of time-varying free-surface profiles in a laboratory wave flume *Coast. Eng.* **68** 1–5
[23] Martins K, Blenkinsopp C E, Power H E, Bruder B, Puleo J A and Bergsma E W J 2017 High-resolution monitoring of wave transformation in the surf zone using a LiDAR scanner array *Coast. Eng.* **128** 37–43
[24] Domino L, Fermigier M, Fort E and Eddi A 2018 Dispersion-free control of hydroelastic waves down to sub-wavelength scale *Eur. Phys. Lett.* **121** 14001
[25] Ono-Dit-Biot J C, Trejo M, Loukiantcheko E, Lauch M, Raphaél K D-V and Salez T 2019 Hydroelastic wake on a thin elastic sheet floating on water *Phys. Rev. Fluids* **4** 014808
[26] Moisy F, Rabaud M and Salsac K 2009 A synthetic schlieren method for the measurement of the topography of a liquid interface *Exp. Fluids* **46** 1021–36
[27] Vien B S, Wong L, Kuen T, Courtney F, Kodikara J and Chiu W K 2020 Strain monitoring strategy of deformed membrane cover using unmanned aerial vehicle-assisted 3D photogrammetry *Remote Sens.* **12** 2738
[28] Marendić A, Gajski D, Duvnjak I and Paar R 2025 Evaluation of photogrammetric methods for displacement measurement during structural load testing *Remote Sens.* **17** 2569
[29] Bolognini M, Izzo G, Marchisotti D, Fagiano L, Limongelli M P and Zappa E 2022 Vision-based modal analysis of built environment structures with multiple drones *Autom. Constr.* **143** 104550
[30] Chen G, Liang Q, Zhong W, Gao X and Cui F 2021 Homography-based measurement of bridge vibration using UAV and DIC method *Measurement* **170** 108683
[31] Deike L, Bacri J and Falcon E 2013 Nonlinear waves on the surface of a fluid covered by an elastic sheet *J. Fluid Mech.* **733** 394–413
[32] Landau L D and Lifshitz E M 1970 *Theory Of Elasticity* 2 edn (Pergamon Ltd)
[33] Schulkes R M S M, Hosking R J and Sneyd A D 1987 Waves due to a steadily moving source on a floating ice plate. Part 2 *J. Fluid Mech.* **180** 297–318
[34] Deike L, Berhanu M and Falcon E 2017 Experimental observation of hydroelastic three-wave interactions *Phys. Rev. Fluids* **2** 064803
[35] Uksul E, Laskari A, Schreier S and Poelma C 2025 Velocity field measurements under very large floating structures interacting with surface waves *Ocean Eng.* **315** 119759
[36] Iijima K, Ma C, Pambela A R and Maeda T 2022 DIC measurement of deflection waves travelling along a thin flexural plate floating at water surface *Ocean Eng.* **266** 113079, 12
[37] Reu P 2014 The art and application of DIC. Calibration: stereo calibration *Exp. Tech.* **38** 1–2
[38] Adrian R J and Westerweel J 2011 *Particle Image Velocimetry* (Cambridge University Press)
[39] Van Rossum G 2009 *Python 3 Reference Manual* (Python Software Foundation)
[40] Virtanen P, Gommers R and Oliphant T E *et al* 2020 SciPy 1.0: fundamental algorithms for scientific computing in python *Nat. Methods* **17** 261–72
[41] Hertz H 1884 Ueber das Gleichgewicht schwimmender elastischer platten *Ann. Phys.* **258** 449–55
[42] Lawson N J and Wu J 1997 Three-dimensional particle image velocimetry: experimental error analysis of a digital angular stereoscopic system *Meas. Sci. Technol.* **8** 1455–64
[43] Turner D Z 2015 Digital image correlation engine (DICe) reference manual *Sandia Report Sand2015-10606 O*
[44] Jones E M C and Iadicola M A 2018 A good practices guide for digital image correlation *Int. Digital Image Correlation Society*
[45] Pot H, Westerweel J and Schreier S 2025 Dataset underlying the publication: stereoscopic digital image correlation for hydroelastic waves of floating membranes *4TU.ResearchData* (https://doi.org/10.4121/3a3f5341-5d75-4caa-96c5-c3f07530f9a5)
[46] Zhang M and Schreier S 2022 Review of wave interaction with continuous flexible floating structures *Ocean Eng.* **264** 112404
[47] Xu P and Wellens P 2022 Fully nonlinear hydroelastic modeling and analytic solution of large-scale floating photovoltaics in waves *J. Fluids Struct.* **109** 103446
[48] Meerkerk M, Poelma C and Westerweel J 2020 Scanning stereo-PLIF method for free surface measurements in large 3D domains *Exp. Fluids* **61** 19
[49] Wu J, Nichols A, Krynkin A and Croft M 2022 Digital image correlation for stereoscopic measurement of water surface dynamics in a partially filled pipe *Acta Geophys.* **70** 2451–67
[50] O'Kiely D, Box F, Kodio O, Whiteley J and Vella D 2020 Impact on floating thin elastic sheets: a mathematical model *Phys. Rev. Fluids* **5** 014003
[51] Duchemin L and Vandenberghe N 2014 Impact dynamics for a floating elastic membrane *J. Fluid Mech.* **756** 544–54
[52] Vandenberghe N and Duchemin L 2016 Impact on floating membranes *Phys. Rev. E* **93** 052801
[53] Keller J B and Miksis M J 1983 Surface tension driven flows *SIAM J. Appl. Math.* **43** 268–77
[54] Reu P 2015 All about speckles: speckle density *Exp. Tech.* **39** 1–2
[55] Reu P 2015 All about speckles: contrast *Exp. Tech.* **39** 1–2